Journal of Physics:
Conference Series

Efficient Compressible Turbulent Flow Simulations: Entropy Projection and Correction for an ILES in a Discontinuous Galerkin solver

To cite this article: E. Carnevali *et al* 2026 *J. Phys.: Conf. Ser.* **3173** 012034

Efficient Compressible Turbulent Flow Simulations: Entropy Projection and Correction for an ILES in a Discontinuous Galerkin solver

E. Carnevali[1], **A. Crivellini**[1], **L. Alberti**[1] **and A. Colombo**[2]

[1]Department of Industrial Engineering and Mathematical Sciences, Marche Polytechnic University, Ancona, Italy
[2]Department of Engineering and Applied Sciences, University of Bergamo, Dalmine, Italy

E-mail: e.carnevali@staff.univpm.it

Abstract. We present the assessment of an entropy projection-correction approach, embedded on a high order discontinuous Galerkin (DG) scheme, as an effective and efficient solution for undertaking under-resolved implicit Large Eddy simulations (iLES) of turbulent transonic/supersonic flows. Combining the L_2 projection of the discrete spatial operators onto the entropy variable space with the residual correction of [1] we achieve an entropy conserving/stable (EC/ES) DG discretization of the convective operators upon suitable choice of the associated numerical flux function. The resulting framework shows an improved robustness which is exploited to tackle iLES on severely under-resolved space discretizations, achieving remarkably accurate solutions even on such coarse computational spaces.

1 Introduction

The idea of exploiting the numerical properties of structure-preserving discretizations to undertake challenging scale-resolving simulations is not new. However, in current literature under-resolved DG simulations are usually performed at low Mach numbers [2, 3, 4, 5], leaving the robustness of the approach under transonic/supersonic conditions questionable. In this contribution, we present the assessment of a modal DG entropy projection-correction method addressing such more demanding scenario.

We show the approach to be an effective and efficient solution for undertaking scale-resolving simulations of turbulent transonic/supersonic flows. The projection operation of the discrete spatial operators onto the entropy variables space guarantees a robustness enhancement with respect to the baseline conservative scheme, enabling to account for both the discretization errors related to the under-resolution and the sharp variations of the thermodynamic state related to supersonic conditions. Furthermore, since the projected state is only used in the evaluation of the spatial operator, the non-stationary term retains its conservative form, hence both guaranteeing the formal conservation of the standard quantities and maintaining a computational cost comparable with the baseline standard (conservative) scheme [6]. On top of this, the introduction of the explicit entropy correction [1] in such entropy-projected framework guarantees an entropy conserving/stable (EC/ES) discretization of the convective term upon suitable choice of the numerical flux function [6].

The solver is tested against some benchmark cases involving the turbulent compressible and near-incompressible channel flows, and the transonic/supersonic flow impinging on a sphere at $Re = 1000$. Concerning the former, our results show that, consistently with the well-known behaviour of Godunov-type methods at low-Mach number [7, 8, 9], the near-incompressible cases benefit from a discretization that enforces a zero production of numerical entropy at the internal faces. In contrast, high-Mach number configurations require a moderate dissipation, introduced via ES fluxes, to achieve "correct" results. We note that the proposed entropy-aware modification yields considerably more accurate solutions compared to previous under-resolved low-Mach channel simulations performed on our baseline modal framework [10], even in face of a lower number of degrees of freedom (DoF) being used in the solution representation. We also provide the numerical proof that the proposed framework can operate with little to no numerical dissipation without stability issues, i.e. aliasing errors, even at extreme under-resolutions. On the other hand, as far as the flow impinging on a sphere is concerned the solver robustness enables to simulate the problem without any additional shock capturing algorithm nor any positivity-preserving limiter, achieving remarkably accurate results in terms of mean flow values upon comparison with the reference DNS dataset [11].

2 Numerical Framework

The system of the governing equations can be written in compact form as

$$\frac{\partial \mathbf{q}}{\partial t} + \frac{\partial \mathbf{F}_{c,i}(\mathbf{q})}{\partial x_i} + \frac{\partial \mathbf{F}_{v,i}(\mathbf{q}, \nabla \mathbf{q})}{\partial x_i} = \mathbf{0}, \tag{1}$$

with $i = 1, \dots, d$, where d is the dimension of the geometrical space, $\mathbf{q}$ is the set of the *conservative* variables, and $\mathbf{F}_c$, $\mathbf{F}_v \in \mathbb{R}^{(2+d)\times d}$ are the convective and viscous flux functions, respectively. The weak formulation of Eq. (1) is obtained by multiplying it by a smooth test function $\mathbf{\Phi} \in \mathbb{R}^{2+d}$ and integrating over the domain $\Omega \subset \mathbb{R}^d$

$$\int_\Omega \mathbf{\Phi}^\top \frac{\partial \mathbf{q}}{\partial t} d\Omega - \int_\Omega \left(\frac{\partial \mathbf{\Phi}}{\partial x_i}\right)^\top \left(\mathbf{F}_{c,i} + \mathbf{F}_{v,i}\right) d\Omega + \int_{\partial\Omega} \mathbf{\Phi}^\top \left(\mathbf{F}_{c,i} + \mathbf{F}_{v,i}\right) n_i d\sigma = 0, \tag{2}$$

where integration by part is exploited and n_i denotes the i-th Cartesian component of the boundary normal unit vector. A well-known feature of system of equations in the form of Eq. (1) is the contraction into an additional conservation equation for an entropy scalar function $\mathcal{S}(\mathbf{q})$, under suitable smoothness conditions, when left-multiplied by a set of entropy variables $\mathbf{v} = \partial\mathcal{S}/\partial\mathbf{q}$, see [12].

Within a DG discretization of Eq. (2), the domain Ω is discretized by means of the mesh $\mathcal{K}_h = \{K\}$, made of cells K, and the functions $\mathbf{q}$ and $\mathbf{\Phi}$ are replaced by the discontinuous finite element approximations $\mathbf{q}_h$ and $\mathbf{\Phi}_h \in [\mathcal{V}_h]^d$, where

$$\mathcal{V}_h = \{\phi \in L_2(\Omega) : \phi|_K \in \mathbb{P}^p_d(K), \forall K \in \mathcal{K}_h\} \tag{3}$$

is the set of piecewise-continuous, p-th degree, d-dimensional polynomial functions. As a basis for $\mathcal{V}_h$, the orthonormal and hierarchical set of functions $\{\phi_l\}_{l=1}^{N_{\mathrm{DoF}}}$ $\forall K \in \mathcal{K}_h$ defined in the mesh space, where $N_{\mathrm{DoF}} = \prod_{\iota=1}^{d}(p+\iota)/\iota$, is used. Any numerical function belonging to the discontinuous polynomial space can be formulated using the elements of a global vector of degrees of freedom (DoF). As an example, the κ-th component of the solution vector $\mathbf{q}_h$ can be expressed as a function of the set of DoF $\mathbf{Q}$ as $\mathrm{q}_{h,\kappa} = \phi_l Q_{\kappa,l}$ $\forall K \in \mathcal{K}_h$, where $l = 1, \dots, N_{\mathrm{DoF}}$.

Hughes et al. [12] showed that the weak formulation of Eq. (2), upon choice of $\mathbf{v}$ as unknown vector, effectively enforces a global constraint on the evolution of $\int_\Omega d\mathcal{S}/dt d\Omega \leq 0$. However, within a Finite Element discretization, since all integrals are evaluated via quadrature rules, the aliasing errors stemming from inexact integration of flux functions, in general rational functions of the solution state, spoils the conservation/stability of entropy at discrete level. To achieve an entropy-aware DG discretization within our modal framework, we adopt the approach outlined in [6]. In detail, the solution is sought for the set of the conservative variables, $\mathbf{q}_h$, but the spatial discretization is evaluated from the L_2-projection of the conservative variables onto the entropy ones $\mathbf{v}_h$ as

$$\int_K \mathbf{v}_h^\top \mathbf{\Phi}_h \, d\Omega = \int_K \mathbf{v}^\top \left(\mathbf{q}_h\right) \mathbf{\Phi}_h \, d\Omega \,, \tag{4}$$

Hence, the DG discretization of the governing equations entails solving for the elements $Q_{\kappa,l}$ such that

$$\int_K \phi_l \frac{\partial q_{h,\kappa}}{\partial t} d\Omega - \int_K \frac{\partial \phi_l}{\partial x_i} F_{\kappa,i}\left(\mathbf{v}_h, \nabla_h \mathbf{v}_h + \mathbf{r}\left(\llbracket \mathbf{v}_h \rrbracket\right)\right) d\Omega + \oint_{\partial\Omega} \llbracket \phi_l \rrbracket \hat{F}_{\kappa,n} \left(\mathbf{v}_h^\pm, \left(\nabla_h \mathbf{v}_h + \eta_F \mathbf{r}_F\left(\llbracket \mathbf{v}_h \rrbracket\right)\right)^\pm\right) d\sigma = 0, \tag{5}$$

where $\llbracket \cdot \rrbracket$ is the jump operator, the superscript $\pm$ denotes the discontinuous values of a function at the two sides of a face shared by two mesh elements, $\hat{F}_{k,n}$ is the normal component of the interface numerical flux and $\mathbf{r}_F\left(\llbracket \mathbf{v}_h \rrbracket\right)$ is the lift operator of the Bassi-Rebay 2 (BR2) viscous scheme computed on the considered boundary face. Concerning the latter, a complete discussion over its provably ES character may be found in [13]; herein, we limit the discussion to the entropy-related behaviour of the convective discrete operator, for which the residual correction is constructed.

Considering the "implicitly" recombined entropy equation, obtained by substituting ϕ_l with $\mathrm{v}_{h,k}$ in Eq. (5), it is easy to derive that the convective volume integral term does not satisfy the following relation

$$\int_K \frac{\partial \psi_{h,i}}{\partial x_i}\, d\Omega = \oint_{\partial K} \psi_{h,i} n_i \, d\sigma \,, \tag{6}$$

since the commutation at discrete level is spoiled by integration errors due to the rational character of $\psi_{h,i}(\mathbf{v}_h)$. The function ψ_i defines, particularly, an entropy potential flux, see [14], defined as

$$\psi_i = \mathbf{v}^\top \mathbf{F}_{c,i} - g_i \tag{7}$$

with g_i being the flux of mathematical entropy $\mathcal{S}$. Notably, $\psi_i = \rho u_i$ upon choice of $\mathbf{v}$ as the one in [12]. The previously mentioned integration error does not allow to retain a discrete convective operator collapsing into the following relation

$$\oint_{\partial K} \left[[\![v_{h,\kappa}]\!] \hat{F}_{\kappa,n} - [\![\psi_{h,i}]\!] n_i \right] d\sigma \geq 0 \,, \tag{8}$$

known as *Tadmor's condition*. In other words, even upon adoption of an EC flux the scheme does not guarantee entropy conservation, not even in the limit of $Re \to \infty$. To account for the integration errors avoiding an exact contraction of the discrete convective term into Eq. (8), the residual correction proposed in [1] is also introduced. Defining the element-wise integration error

$$\alpha_K = \int_\Omega \frac{\partial \psi_{h,i}}{\partial x_i} d\Omega \; - \; \oint \psi_{h,i} n_i \, d\sigma \tag{9}$$

and adding it on the left hand side of Eq. (5) as

$$\alpha_K \frac{\int_K \phi_l \overline{\mathbf{v}}_h d\Omega}{\int_K \overline{\mathbf{v}}_h^\top \overline{\mathbf{v}}_h d\Omega} \,, \tag{10}$$

where the definition $\overline{\mathrm{v}}_{h,\kappa} = \phi_l V_{\kappa,l} - \phi_1 V_{\kappa,1}$ ensures the correction to be passive only on the first, average-containing DoF of each equation. It is easy to then derive that the resulting DG discretization is globally ES/EC depending on the choice of the convective interface numerical flux. Notably, the orthonormality of the compactly defined base functions ϕ_l greatly simplifies the correction distribution operation represented by Eq. (10), as the denominator simply collect the L_2 norm of the average-free solution state, while the numerator effectively extract the $l-$th DoF of each solution state component$\mathrm{V}_{\kappa,l}$ for $l > 1$.

3 Numerical Results

3.1 Channel flows

The incompressible reference cases at $Re_\tau = \{180,\, 395,\, 590\}$ are taken from the DNS dataset of [15]. The three Cartesian subdivisions adopted for the near-incompressible simulations are $i)$ $8 \times 8 \times 6$ for $Re_\tau = 180$, $ii)$ $8 \times 8 \times 8$ for $Re_\tau = 395$, $iii)$ $12 \times 12 \times 12$ for $Re_\tau = 590$, see Tab. 1. For these cases the numerical dissipation of the framework is minimized by setting the jump penalization coefficient as $\eta_F = 1$. On the other hand, to provide adequate dissipation at the boundaries, a local value $\eta_{F,w} = 8$ is adopted. Concerning instead the convective flux discretization, both the exact ES Riemann solver [16] and the EC flux of Ismail and Roe [17] are used. The results drawn from such implementations are outlined in Fig. 1 , where we report the mean velocity profiles and the corresponding Reynolds stress components for all the different configurations. It is easy to observe that our EC low-dissipation framework significantly enhances the accuracy with respect to a standard ES implementation. Particularly, the adoption of the EC flux allows to accurately evaluate the wall-normal behavior of τ_{13}, i.e. the relevant quantity to be accurately captured to produce good results, whereas the use of the ES flux always results in an over-shearing of the turbulent fluctuations in the viscous layer. Notably, the peak turbulent production $-\langle u_1' u_3' \rangle \partial \langle u_1 \rangle / \partial x_3$ typically occurs within the buffer region of the viscous layer; as such, an under/over-prediction of turbulent fluctuations in this region has a significant impact on the overall structure of the mean flow.

Moving to the compressible channel flows, see Tab. 2, the chosen benchmark cases are the configurations characterized by $Re_\tau = \{222,\, 500,\, 1000\}$ at $M_b = 1.5$ and the case $Re_\tau = 450$ at $M_b = 3$, with M_b identifying a bulk-average Mach number. All the reference solutions are taken from the DNS dataset of [18]. The mappings of [19], applied to scale-resolved DG solutions of the previously reported compressible flows [20], allowed to identify a collapsing of the compressible mean velocity profiles onto the equivalent incompressible ones reported in Fig. 2. The observed results justifies the extension of the computational meshes adopted in the low-Mach iLES

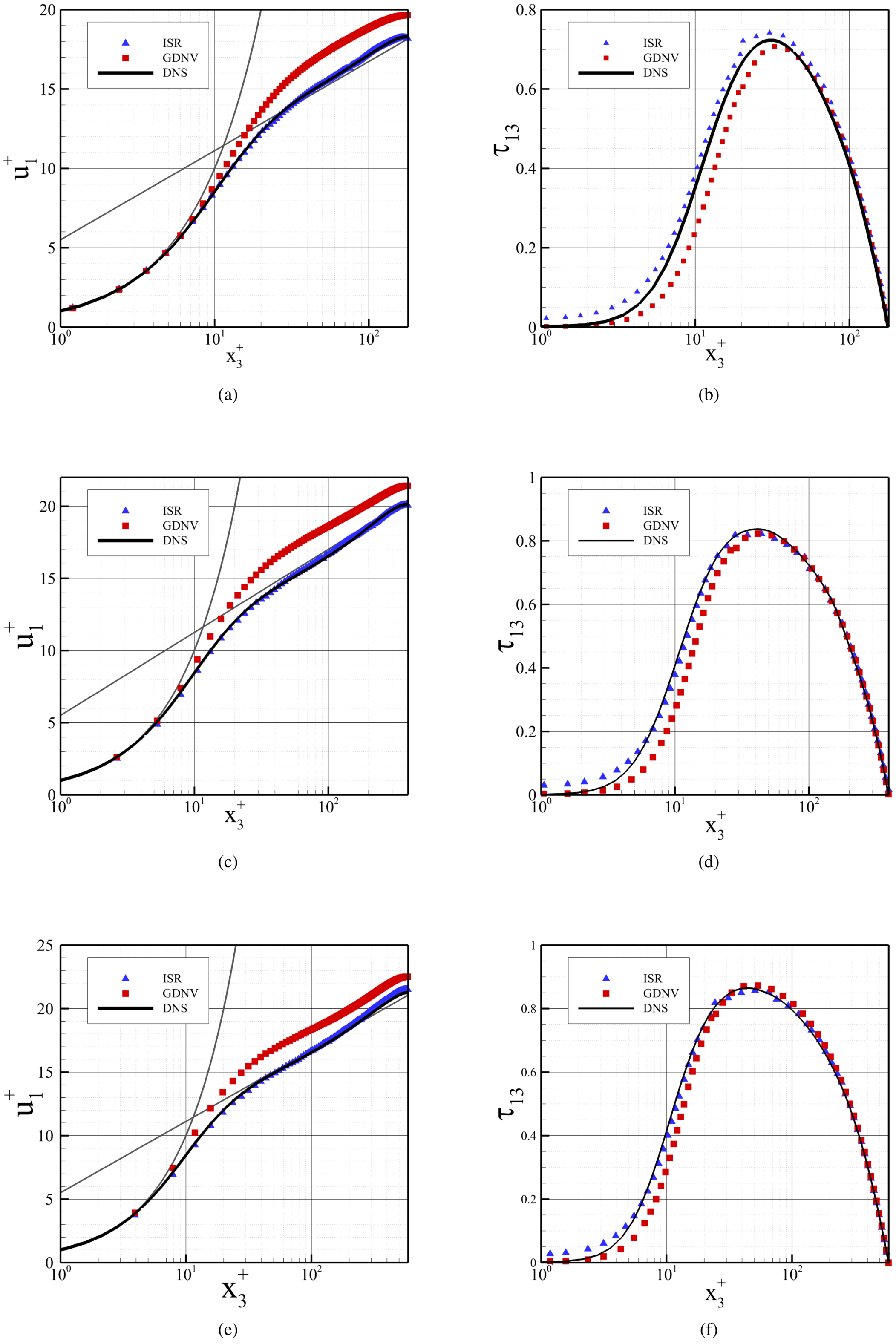

(a) (b)

(c) (d)

(e) (f)

Figure 1: Mean velocity profile and mean Reynolds stresses for the incompressible channel flows at $Re_\tau = 180$ (first row), $Re_\tau = 395$ (second row) and $Re_\tau = 590$ (third row). Results reported at polynomial order $p = 6$. Implementation of ES Godunov flux (■) and EC Ismail-Roe flux (▲). DNS data (——) from [15].

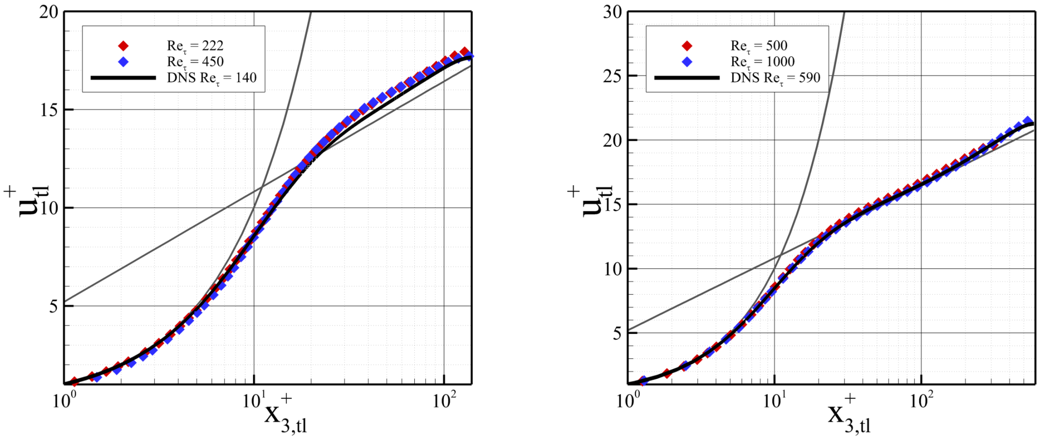

(a) (b)

Figure 2: Trettel-Larsson transformation applied to DG scale-resolved compressible solutions at polynomial order $p = 8$.

to the aforementioned compressible configurations. Particularly, as the cases at $Re_\tau = 222$ and $Re_\tau = 450$ collapse onto the $Re_\tau = 140$ incompressible profile, we use for these the same computational mesh of the near-incompressible case at $Re_\tau = 180$. The obtained results are reported in Fig. 3 and 4.

Starting from the results portrayed in Fig. 3, the overall trend shows a greater accuracy of the ES flux on coarse space resolutions. For the $Re_\tau = 222$ case, we note that an accuracy improvement is obtained by decreasing the interface jump penalization coefficient to $\eta_F = 1$. The adoption of a convective flux with inbuilt upwind structure, as Godunov-type flux are, leads to significantly more accurate results for high-Mach number flows with respect to centred convective discretizations. As far as the $M_b = 3$ case is concerned, see Fig. 4, some additional comments are required. While the reference DNS computations [18] adopt a Sutherland model for the viscosity, a power-law model is instead used in the present DG computations. As long as the temperature remains sufficiently close to its reference value, the difference in the predicted viscosity among the two models is fairly negligible. On the other hand, the $M_b = 3$ case presents a significant temperature gradient developing in the wall-normal direction. As such, some deviation emerged between the derived scale-resolved DG solution and the reference dataset [18]. To obviate, the iLES result is compared with a reference solution which is the corresponding scale-resolved DG dataset.

Considering the iLES solution in Fig. 4, we first note that the straightforward application of the EC flux resulted in an abrupt crash of the simulations. As such, the Ismail-Roe flux required the addition of a Rusanov-like upwind bias as

$$-\beta \frac{\max(|\lambda_K^+|, |\lambda_K^-|)}{2} [\![\mathbf{q}(\mathbf{v}_h^\pm)]\!] , \tag{11}$$

where λ_K is the largest convective eigenvalue and β is a scalar relaxation factor, here set to 0.3. Clearly, the baseline ES implementation provides a result which gets very close to the scale-resolved DG reference solution, despite the significant under-resolution. Oppositely, the upwind-biased EC flux underpredicts the resolved velocity profile and, consistently, is characterized by an excessive turbulent shear stress τ_{13} in the near-wall region. Also, for this case the implementation of the biased EC flux still requires the introduction of the DEEB correction to successfully complete the simulation, signalling its stabilizing effect on the solver.

In Fig 5 we further plot the turbulent kinetic energy distribution along the wall-normal direction for the two cases presenting the larger under-resolution with respect to the reference DNS; these, particularly, are the incompressible $Re_\tau = 590$ and the high-Mach number case at $Re_\tau = 1000$. Upon inspection of Fig. 5(a) it is clearly noticeable the strong discontinuous character of the solution in the near-incompressible regime with the EC flux, as the coupling of a centered flux with a unitary-value penalization of the jump discontinuities leads to a strongly oscillating solution. For the compressible case, e.g. Fig. 5(b), we note that since the penalization coefficient is increased the EC solution assumes a significantly smoother profile, although sensibly undershooting the DNS reference. On the contrary, the ES flux over-predicts the peak turbulent kinetic energy despite showing a sensibly more accurate mean velocity profile.

Finally, the under-resolution aspect is further stressed by considering the two cases $Re_\tau = \{500, 1000\}$ at $M_b = 1.5$ adopting the grids $6 \times 6 \times 6$ and $8 \times 8 \times 8$, respectively. The obtained results are portrayed in Fig 6.

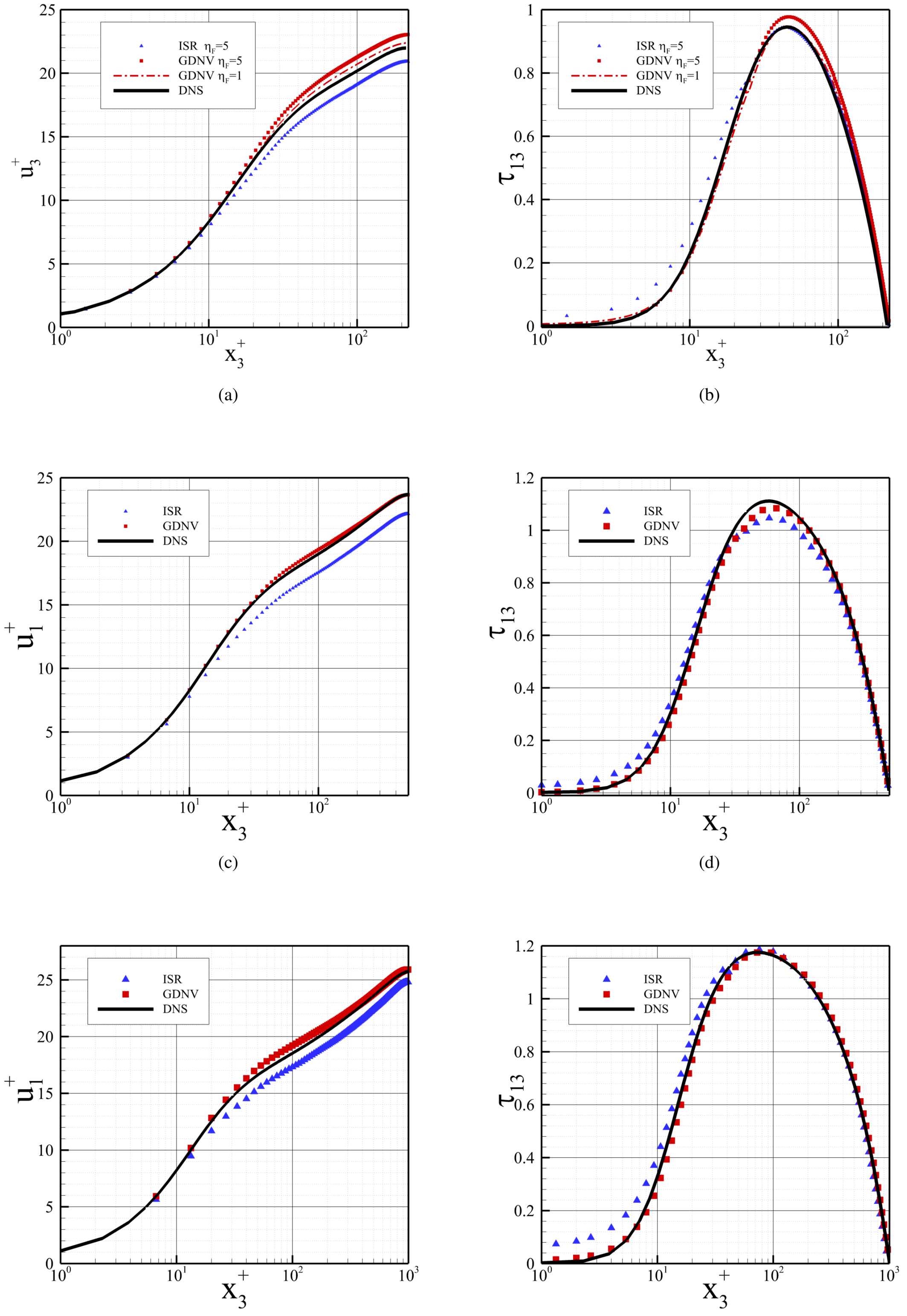

(a) (b)

(c) (d)

(e) (f)

Figure 3: Mean velocity profile and mean Reynolds stresses for the $M_b = 1.5$ compressible channel flows at $Re_\tau = 222$ (first row), $Re_\tau = 500$ (second row) and $Re_\tau = 1000$ (third row). Results reported at polynomial order $p = 8$. Implementation of ES Godunov flux (🟥) and EC Ismail-Roe flux (▲). DNS data (——) from [18]

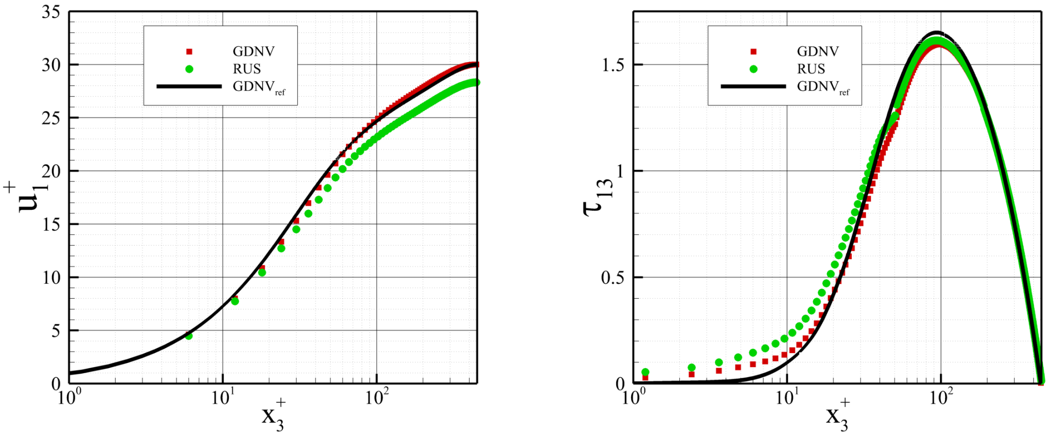

(a) (b)

Figure 4: Mean velocity profile and mean Reynolds stresses for the $M_b = 3$ compressible channel flows at $Re_\tau = 450$. Results reported at polynomial order $p = 8$. Implementation of ES Godunov flux (🟥) and upwind-biased Ismail-Roe flux (●). DNS data (——) from [18]

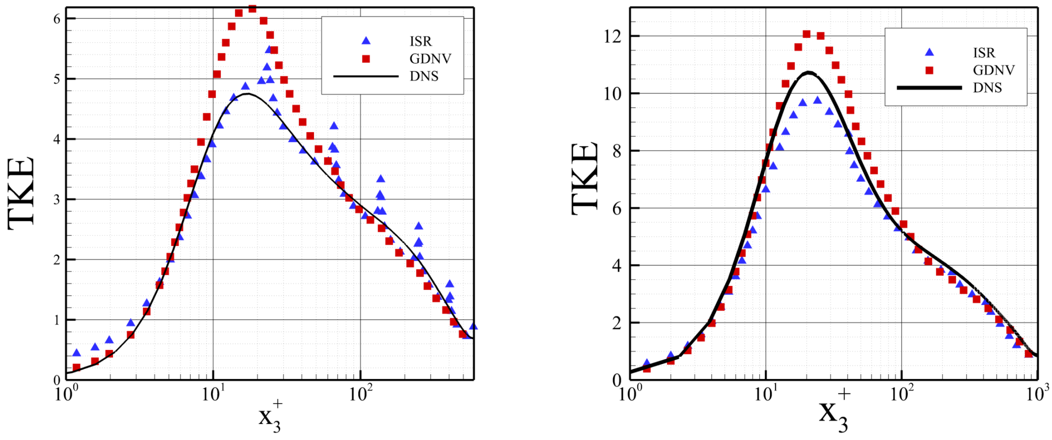

(a) (b)

Figure 5: Turbulent kinetic energy $TKE = \frac{\langle u_1' u_1' \rangle + \langle u_2' u_2' \rangle + \langle u_3' u_3' \rangle}{2}$. (a) Incompressible channel flow, $Re_\tau = 590$. (b) $M_b = 1.5$ channel flow, $Re_\tau = 1000$. Implementation of ES Godunov flux (🟥) and the EC Ismail-Roe flux (▲). DNS data (——) from [15, 18].

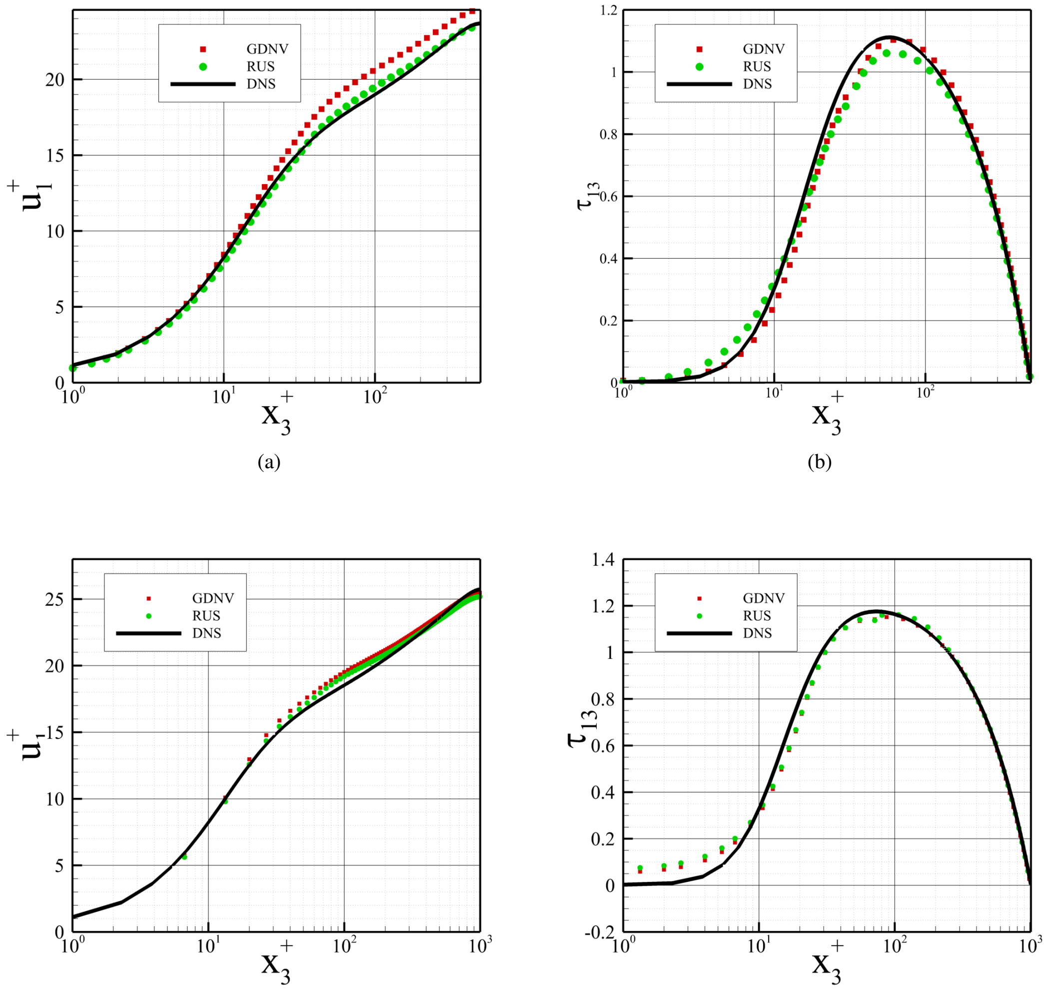

(a) (b)

(c) (d)

Figure 6: Compressible channel flows at $M_b = 1.5$. $Re_\tau = 500$ (top row) and $Re_\tau = 1000$ (bottom row). Solutions at polynomial order $p = 8$. Implementation of ES Godunov flux (🟥) and upwind-biased Ismail-Roe flux (●). DNS data (——) from [18]

Solutions are reported considering the ES Godunov flux and the upwind biased EC flux of Ismail and Roe. For the latter, the adopted coefficients for the two simulations $Re_\tau = \{500,\ 1000\}$ are $\beta = \{0.1,\ 0.3\}$ respectively. We note that the a simple bias modulation considerably improve the solution accuracy for the $Re_\tau = 500$ case, whilst only achieving the same accuracy of the ES flux for the $Re_\tau = 1000$ case.

3.2 *Sphere*

Two cases at freestream Mach values of $M = \{0.95,\ 1.2\}$ are considered, employing a mesh of ≈ 20.000 elements. The computational domain spans the region $-24D \leq z \leq 10D$ and $-10D \leq x, y \leq 10D$, where D denotes the sphere diameter and z represents the streamwise flow direction. On top of providing an additional robustness benchmark test, this case shows the geometrical flexibility of the framework, which may be straightforwardly extended to curved boundary geometries while retaining high accuracy. Figure 7 reports the instantaneous solution fields in terms of λ_2 isocontours coloured by M. Both the laminarization effect and the transition from a weak oblique shock to a detached bow shock ahead of the sphere, are clearly noticeable as the Mach number

Table 1: Summary table of under-resolved near-incompressible channel flow cases. p is the polynomial order, N_e is the number of elements, N_{DoF} is the number of DG DoF and r is the DNS-to-DG DoF ratio. DNS data from [15].

	Re_τ	$N_{x_1} \times N_{x_2} \times N_{x_3}$	p	$N_e\, N_{DoF}$	r
$M_b = 0.18$	180	$8 \times 8 \times 6$	6	32.256	65.5
	395	$8 \times 8 \times 8$	6	43.008	220.6
	590	$12 \times 12 \times 12$	6	145.152	261.0

Table 2: Summary table of under-resolved compressible channel flow cases. In order, p is the polynomial order, N_e is the number of elements, N_{DoF} is the number of DG DoF and r is the DNS-to-DG DoF ratio. DNS data from [18].

	Re_τ	$N_{x_1} \times N_{x_2} \times N_{x_3}$	p	$N_e\, N_{DoF}$	r
$M_b = 1.5$	222	$8 \times 8 \times 6$	8	63.360	176.0
	500	$8 \times 8 \times 8$	8	84.480	265.6
	1000	$12 \times 12 \times 12$	8	285.120	625.8
$M_b = 3.0$	450	$8 \times 8 \times 6$	8	63.360	1412.3

is increased. Figure 8, portraying the behaviour of the transversal force coefficients for the two cases, offers an alternative visualization of the effect of M on the wake structure. Whilst for $M = 0.95$ the orbit drawn by the force coefficients suggests no preferred shedding direction, for the $M = 1.2$ case it is clearly visible a force trajectory which is consistent with a von Kárman-like vortex shedding.

Finally, on Fig. 9 are reported the turbulent kinetic energy spectra for the two cases. The points are located on planes at different axial coordinates z/D from the sphere. In Fig. 9 are reported both the average spectra, computed as average among the spectra of the points at a given z/D, together with pointwise evaluations on the origin of the considered planes. Turbulent transition may be identified for the $M = 0.95$ case, together with the shedding frequency of the $M = 1.2$ case. A compact report of the DG results may be observed in Tab. 3. These appears in good agreement with the DNS reference data of [11], where values of $St = \{0.179,\, 0.169\}$ and $\overline{C}_D = \{0.94,\, 1.05\}$ may be extracted for the two cases at $M = \{0.95,\, 1.2\}$ respectively. It is worth noting that the DG simulation of the $M = 1.2$ case shows a moderate discrepancy from the DNS dataset in terms of computed shedding frequency. Increasing the polynomial order of the DG approximation to $p = 6$ did not produce any significant changes in either the mean flow field or the Strouhal number, indicating convergence of the results. On top of such observation it is also worth pointing out that extending the simulations to the other cases presented in [11] we derived substantial agreement with the results therein reported, in terms of both $\overline{C}_D$ and St. As such, the deviation of the $M = 1.2$ case deserves some additional investigation.

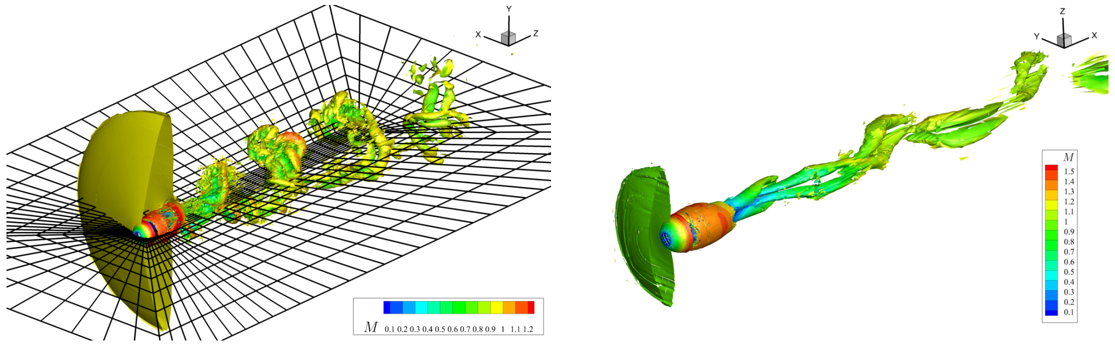

(a) (b)

Figure 7: $Re = 1000$ flow impinging on a sphere. Instantaneous λ_2 isocontours coloured by Mach number. 7(a) $M = 0.95$, solution at polynomial order $p = 6$; 7(b) $M = 1.2$, solution at polynomial order $p = 4$.

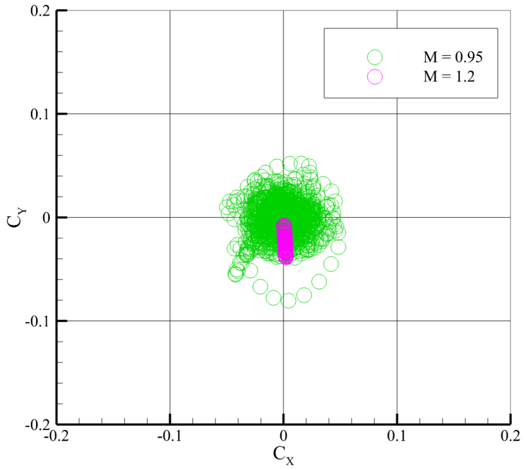

Figure 8: Transversal force coefficient behaviour in the $(C_x - C_y)$ phase plane.

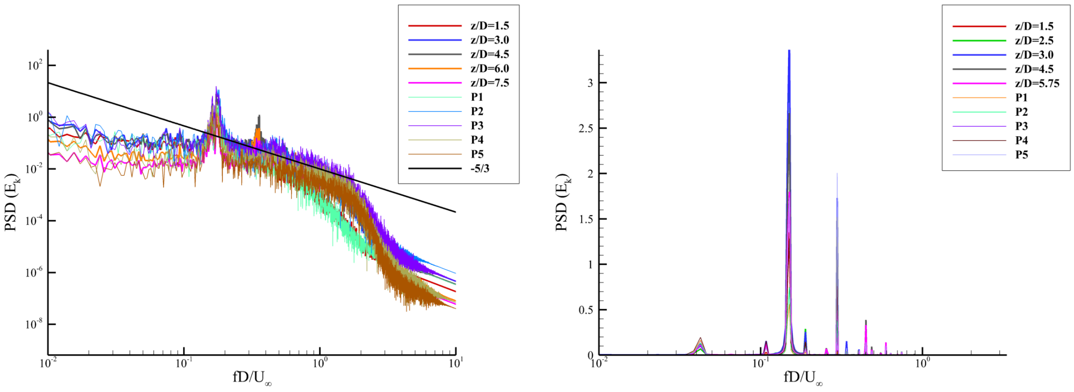

(a) (b)

Figure 9: Caption

	St	$\overline{C}_D$
$M = 0.95$	0.175	0.92
$M = 1.2$	0.150	1.06

Table 3: DG results for the cases at $M = 0.95$ and $M = 1.2$.

4 Conclusions

The structure of the adopted numerical DG framework makes the embedding of an entropy projection-correction strategy virtually inexpensive whilst guaranteeing a significant enhancement of the robustness over the baseline scheme. The improved robustness deriving from the entropy-aware modification allows to successfully undertake highly challenging scenarios, ranging from high-Mach turbulent channel flows to configurations characterized by more complex geometries and flow discontinuities, i.e. shocks , such as the case of a transonic/supersonic flow impinging on a sphere. The favourable dissipation/dispersion properties of the DG method are fully exploited to perform such simulations using a small fraction of the DOFs employed by the reference DNS [18, 11].

References

[1] Rémi Abgrall, Philipp Öffner, and Hendrik Ranocha. Reinterpretation and extension of entropy correction terms for residual distribution and discontinuous Galerkin schemes: application to structure preserving discretization. *Journal of Computational Physics*, 453:110955, 2022.

[2] Gregor J. Gassner and Andrea D. Beck. On the accuracy of high-order discretizations for underresolved turbulence simulations. *Theoretical and Computational Fluid Dynamics*, 27(3):221–237, 2013.

[3] Gregor J Gassner, Andrew R Winters, and David A Kopriva. Split form nodal discontinuous Galerkin schemes with summation-by-parts property for the compressible Euler equations. *Journal of Computational Physics*, 327:39–66, 2016.

[4] David Flad, Andrea Beck, and Claus-Dieter Munz. Simulation of underresolved turbulent flows by adaptive filtering using the high order discontinuous Galerkin spectral element method. *Journal of Computational Physics*, 313:1–12, 2016.

[5] SM Murman and C Frontin. Analysis of numerical dissipation in entropy-stable schemes for turbulent flows. In *Center for Turbulence Research, Proceedings of the Summer Program*, 2018.

[6] Luca Alberti, Emanuele Carnevali, Alessandro Colombo, and Andrea Crivellini. An entropy conserving/stable discontinuous Galerkin solver in entropy variables based on the direct enforcement of entropy balance. *Journal of Computational Physics*, 508, 7 2024.

[7] Hervé Guillard and Cécile Viozat. On the behaviour of upwind schemes in the low Mach number limit. *Computers & fluids*, 28(1):63–86, 1999.

[8] Ben Thornber, Andrew Mosedale, and Dimitris Drikakis. On the implicit large eddy simulations of homogeneous decaying turbulence. *Journal of Computational Physics*, 226(2):1902–1929, 2007.

[9] Ben Thornber, Dimitris Drikakis, Robin JR Williams, and David Youngs. On entropy generation and dissipation of kinetic energy in high-resolution shock-capturing schemes. *Journal of Computational Physics*, 227(10):4853–4872, 2008.

[10] Alessandra Nigro, Carmine De Bartolo, Andrea Crivellini, Matteo Franciolini, Alessandro Colombo, and Francesco Bassi. A low-dissipation DG method for the under-resolved simulation of low Mach number turbulent flows. *Computers & Mathematics with Applications*, 77(6):1739–1755, 2019.

[11] T Nagata, Taku Nonomura, S Takahashi, and K Fukuda. Direct numerical simulation of subsonic, transonic and supersonic flow over an isolated sphere up to a Reynolds number of 1000. *Journal of Fluid Mechanics*, 904:A36, 2020.

[12] Thomas JR Hughes, Leopaldo P Franca, and Michel Mallet. A new finite element formulation for computational fluid dynamics: I. symmetric forms of the compressible Euler and Navier-Stokes equations and the second law of thermodynamics. *Computer methods in applied mechanics and engineering*, 54(2):223–234, 1986.

[13] Luca Alberti, Emanuele Carnevali, Alessandro Colombo, and Andrea Crivellini. Continued development of an entropy-aware high-order modal discontinuous galerkin solver for the navier–stokes equations. *Computers & Fluids*, page 106730, 2025.

[14] Eitan Tadmor. Entropy stability theory for difference approximations of nonlinear conservation laws and related time-dependent problems. *Acta Numerica*, 12:451–512, 2003.

[15] Robert D Moser, John Kim, and Nagi N Mansour. Direct numerical simulation of turbulent channel flow up to $Re_\tau = 590$. *Physics of fluids*, 11(4):943–945, 1999.

[16] Sigal Gottlieb. On high order strong stability preserving Runge-Kutta and multi step time discretizations. *Journal of scientific computing*, 25:105–128, 2005.

[17] Farzad Ismail and Philip L Roe. Affordable, entropy-consistent Euler flux functions ii: Entropy production at shocks. *Journal of Computational Physics*, 228(15):5410–5436, 2009.

[18] Davide Modesti and Sergio Pirozzoli. Reynolds and Mach number effects in compressible turbulent channel flow. *International Journal of Heat and Fluid Flow*, 59:33–49, 2016.

[19] Andrew Trettel and Johan Larsson. Mean velocity scaling for compressible wall turbulence with heat transfer. *Physics of Fluids*, 28(2), 2016.

[20] Luca Alberti, Emanuele Carnevali, Alessandro Colombo, and Andrea Crivellini. An entropy-aware discontinuous galerkin solver for implicit large eddy simulations of wall-bounded flows. *Physics of Fluids*, 37(7), 2025.